Computational Studies Compared to Electrochemical Measurements of Intercalation of Cationic Compounds in Wyoming Montmorillonite

Sungho Park, Alanah Fitch,* and Yunlong Wang

Department of Chemistry, Loyola University of Chicago, Chicago, Illinois 60626

Received: January 8, 1997; In Final Form: March 12, 1997[⊗]

Lattice energy minimizations and molecular dynamics calculations for a selected series of metal complexes with similar metal centers and ligand geometry were performed and were compared to experimental measurements of shifts in redox potentials observed when the complexes are intercalated into negatively charged Wyoming montmorillonite. An excellent correlation between computational trends and experimental trends was observed for nonequilibrium measurements. The results are not dependent on the size of the metal complex or the absolute magnitude of the interaction with the clay surface, but are related to the relative electrostatic energies of the reduced and oxidized complexes. The results are strongly influenced by the distribution of charge within the complex.

Introduction

Molecular transport in porous clay media is of fundamental interest for several reasons. Clay materials are used commercially in filtration processes (separations)[1−3] and environmentally as filtration and fluid flow barriers (landfills).[4−6] There has also been significant interest in using clays as supports for nanostructure devices (electronic and microseparation devices).[7−10] In all of these applications the mechanism of transport is affected by the clay structure and charge[11,12] and by the probe molecular shape, charge, and constituent atoms,[13] as well as by the presence of other molecular species.[14] In addition to these parameters, measurement of transport within clay films depends strongly on the degree of loading of the clay.[15] These points are illustrated in Figure 1. The clay surface can have specific adsorption sites, the energetics of which depend upon coadsorbates. At further distances from the surface a delocalized electric field weakly retains cationic solutes. The equilibrium state for an intercalated cation may be in such an adsorbate−adsorbate well. Consequently, transport occurring under nonequilibrium conditions will be significantly different from transport occurring under equilibrium conditions.

Depending upon the nature of the application, either nonequilibrium or equilibrium transport can be most important. An electrochemical sensor that depends upon mobility of the probe molecule within the clay film would perform most successfully under nonequilibrium conditions, while a landfill might be optimized for equilibrium transport. Nonequilibrium transport studies require a mechanism of flooding the clay and watching the probe advance on a microscopic scale. *Experimentally*, thin films (5 μm dry) of clay can be spin coated over a small underlying electrode to form a single clay particle, such that nonequilibrium transport, as measured by arrival at the underlying electrode, is dominated by between clay layer forces.[16,17] *Theoretically*, equilibrium and nonequilibrium effects can be investigated by computational methods. Modeling of a single molecule sandwiched by two clay surfaces in a unit cell most closely imitates transport under nonequilibrium situations where transport is dominated by unloaded clays. Computational methods have been used to investigate molecular interactions at zeolites.[18,19] Clays have also been modeled to determine adsorption of hydrocarbons.[20−25]

The goal of this investigation is to verify the relationship between computational studies of molecular interaction between a molecule and clay surfaces and experimental results of nonequilibrium transport as measured by clay-modified electrodes (CMEs). The probe molecules to be studied should be those that are identified as being least impacted by loading effects and by probe−probe effects. In other words, the interaction between the probe molecule and the clay should be dominated by long-range electrostatic field effects. Probe molecules whose nonequilibrium penetration of thin clay films approaches this criterion are the series $Ru(NH_3)_6^{3+}$, $Co(NH_3)_6^{3+}$, $Co(en)_3^{3+}$, and $Co(sep)^{3+}$. The experimental results associated with these probe molecules have been detailed elsewhere.[13]

This series of complexes has been further chosen because of the close similarity of the probe molecules (metal center and nitrogen ligands). This similarity will allow us to make correlations between trends in the computations even when assumptions in the modeling (for example, a dielectric model of the clay interlayer instead of an explicit introduction of all water molecules) preclude direct confirmation of computations of a single probe in a unit cell.

Materials and Methods

Standard Wyoming sodium montmorillonite (SWy-1) was obtained from the Source Clays Repository (University of Missouri, Columbia, MO) and purified.[26] Co(sepulchrate)Cl_3 (Co(sep)) (Aldrich), $Ru(NH_3)_6Cl_3$ and Co(ethylenediamine)$_3$-Cl_3 (Co(en)$_3^{3+}$) (Alfa-Aesar), and $Co(NH_3)_6Cl_3$ (Johnson Matthey) were used as received. Co(bipyridine)$_3$(ClO_4)$_3$ (Co-(bpy)$_3^{3+}$) was synthesized as previously described.[12]

Electrodes were polished using 0.05 μm alumina and copious amounts of water. The electrodes were then rinsed and sonicated to remove any remaining alumina. This procedure was performed prior to the addition of clay for the CME and prior to the beginning of any run for the bare electrode. Spin-coated clay-modified electrodes (SPCMEs) were prepared by applying 1 μL of a 35 g/L clay solution to the electrode. The electrode was inserted into an inverted Pine MSR electrode rotator and spun at 800 rpm for 20 min. Electrodes were visually inspected for cracks. Those with cracks were discarded, and a new clay film was applied. Acceptable films were allowed to preswell for 5 min in the N_2-purged electrolyte and then switched to the same electrolyte containing the probe molecule. An SCE and a Pt wire were used as reference and counter electrodes, respectively.

Electrochemistry was carried out in a standard three-electrode configuration with an AgCl/Ag used as a reference electrode.
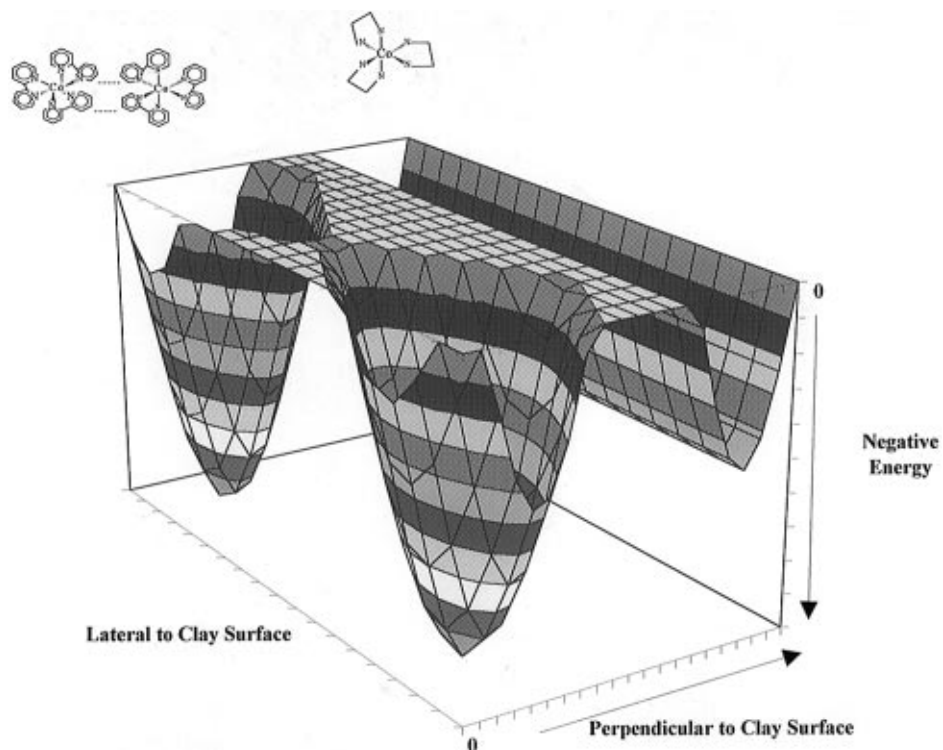

Figure 1. Delocalized electric field driven energy channel and adsorbate−adsorbate driven energy well at a clay surface.
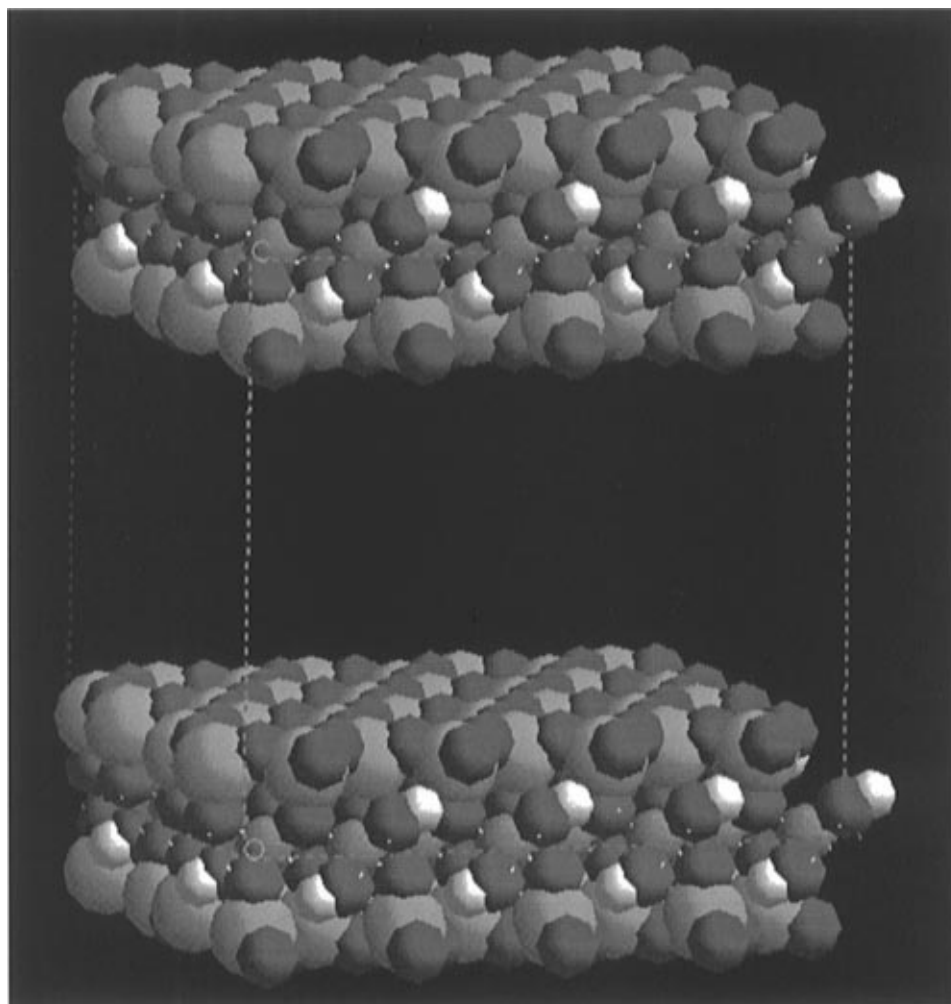

Figure 2. Montmorillonite clay model, the simulation unit lattice structure containing eight (4 × 2) unit cells from the X-ray structure.

A PAR 175 universal programmer and a PAR 173 potentiostat (EG&G) were used with data collected to a Gateway 486 using a Cio-Das08 A/D converter (Computer Boards, Inc., MA) and Snap-Master Data acquisition software (HEM Data Corp, MI) for data collection. Multiple sweep cyclic voltammograms were obtained at a concentration of 1 mM probe and 0.1 M NaCl

Intercalation of Cationic Compounds in Montmorillonite

J. Phys. Chem. B, Vol. 101, No. 25, 1997 **4891**

and a sweep rate of 50 mV/s between the potentials of 0.4 V and -0.8 V for $Co(en)_3^{3+}$, 0.5 V and -0.5 V for $Ru(NH_3)_6^{3+}$, and 0 V and -0.8 V for $Co(sep)^{3+}$.

Computational Methods

Clay Model. The clay montmorillonite that we have studied is based on natural Wyoming montmorillonites. The ideal formula for this type of dioctahedral smectite clay when there is no metal atom substitution is $Al_4Si_8O_{20}(OH)_4$. We used a well-known ideal isomorphic substituted formula for the clay montmorillonite.[27]

$$[Si_{7.75}Al_{0.25}][Al_{3.5}Mg_{0.5}]O_{20}(OH)_4 \quad (1)$$
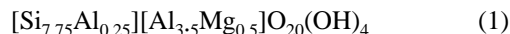
Our simulation unit cell contains 8 ($4 \times 2 \times 1$, *xyz*) unit cells for montmorillonite clay, obtained from X-ray data.[28] A slab size of 21.12 Å by 18.28 Å by 6.56 Å of clay was used (Figure 2). Our 4×2 model bears negative charge of six electrons (two electrons from substituted Al in the tetrahedral position of Si and four electrons from substituted Mg in the octahedral position). This corresponds to the negative charge of 0.375 electrons per formula unit of $Al_2Si_4O_{10}(OH)_2$, and it also satisfies the requirement of natural Wyoming montmorillonite bearing a negative charge of 0.25−0.6 electrons for the same formula.[29,30] A complete 2:1 layer containing an octahedral aluminum oxide layer sandwiched by two silicon oxide layers was used. The charge of each of the atoms in the structure was assigned on the basis of previous works.[31,32] The substitutional disorder for the constructed $4 \times 2 \times 1$ clay model was carried out within the Cerius 2 molecular simulation software package to consider the negative charge of clay due to its isomorphic substitutions in the octahedral Al^{3+} by Mg^{2+} and in the tetrahedral Si^{4+} by Al^{3+}. The interatomic potentials for clay to metal complex were obtained from the parametrized universal force field (UFF) without attempting any separate quantum energy parametrization due to the large numbers of the atoms in the metal complex of interest with respect to the clay fragment.

The total energy of the system, in which a metal complex is interacting with the clay surface, is expressed as a sum of bonded interactions and nonbonded interactions:

$$E_{total} = E_{bonded} + E_{nonbonded} \quad (2)$$

The bonded interactions consist of bond stretching, bond angle bending, dihedral angle torsion, and inversion terms.

$$E_{bonded} = E_{bond} + E_{ang} + E_{torsion} + E_{inversion} \quad (3)$$

The nonbonded interactions consist of electrostatic (Coulombic) and van der Waals terms.

$$E_{nonbonded} = E_{coul} + E_{vdw} \quad (4)$$

The electrostatic energy is given by

$$E_{coul} = C_0 \sum_i \sum_{j>i} (Q_i/Q_j) \epsilon R_{ij} \quad (5)$$

where Q_i and Q_j are atomic charges in electron units (Table 1), R_{ij} is the distance between atoms in Å, ϵ is the dielectric constant ($\epsilon_0 = 1$ for vacuum), and C_0 is a conversion factor (332.0637), resulting in E_{coul} in kcal/mol.[32]

Lennard-Jones 12-6 potentials are used for the van der Waals interaction:

$$E_{vdw}(r) = D_0[(R_0/R)^{12} - 2(R_0/R)^6] \quad (6)$$

TABLE 1: Atomic Charge (*e*) of the Clay Atoms in the Fragment and Their Cartesian Coordinates (Å)

atom	x	y	z	charge
O1	2.6400	0.0000	3.2800	−0.800
O2	1.3200	2.2800	3.2800	−0.800
O3	3.9600	2.2800	3.2800	−0.800
O4	5.2800	0.0000	1.0601	−1.717
H5	6.1615	0.0000	1.4341	0.717
Si6	2.6400	1.5200	2.7300	1.200
Si7	0.0000	3.0500	2.7300	1.200
O8	2.6400	1.5200	1.0601	−1.000
O9	0.0000	3.0500	1.0601	−1.000
Al10	4.4000	1.5200	0.0000	3.000
Al11	4.4000	7.6200	0.0000	3.000
O12	0.0000	4.5700	3.2800	−0.800
O13	3.9600	6.8500	3.2800	−0.800
O14	1.3200	6.8500	3.2800	−0.800
O15	2.6400	4.5700	1.0601	−1.717
H16	3.5215	4.5700	1.4341	0.717
Si17	0.0000	6.0900	2.7300	1.200
Si18	2.6400	7.6200	2.7300	1.200
O19	0.0000	6.0900	1.0601	−1.000
O20	2.6400	7.6200	1.0601	−1.000
Al21	1.7600	6.0900	0.0000	3.000
Al22	1.7600	3.0500	0.0000	3.000
O23	0.8800	0.0000	−3.2800	−0.800
O24	2.200	6.8600	−3.2800	−0.800
O25	4.8400	6.8600	−3.2800	−0.800
O26	3.5200	0.0000	−1.0601	−1.717
H27	2.6385	0.0000	−1.4341	0.717
Si28	0.8800	7.6200	−2.7300	1.200
Si29	3.5200	6.0900	−2.7300	1.200
O30	0.8800	7.6200	−1.0601	−1.000
O31	3.5200	6.0900	−1.0601	−1.000
O32	3.5200	4.5700	−3.2800	−0.800
O33	4.8400	2.2900	−3.2800	−0.800
O34	2.2000	2.2900	−3.2800	−0.800
O35	0.8800	4.5700	−1.0601	−1.717
H36	0.0015	4.5700	−1.4341	0.717
Si37	3.5200	3.0500	−2.7300	1.200
Si38	0.8800	1.5200	−2.7300	1.200
O39	−3.5200	3.0500	−1.0601	−1.000
O40	0.8800	1.5200	−1.0601	−1.000

TABLE 2: van der Waals Parameters in Eq 6

atom	R_0 (Å)	D_0 (kcal/mol)
Co	2.8720	0.0140
Ru	2.9630	0.0560
N	3.6600	0.0690
C	3.8510	0.1050
H	2.8860	0.0440
Al	4.4990	0.5050
Si	4.2950	0.4020
O	3.5000	0.0600

where D_0 is the bond strength (well depth) in kcal/mol, R_0 is the equilibrium bond length in Å, and R is the bond length in Å. The values of the parameters in eq 6 for the atoms in the clay are given in Table 2.

An Ewald summation was carried out for the long-range corrections of the electrostatic potential necessary to avoid border artifacts.[33] This method converts the Coulomb and dispersion terms into two different summations (one in real space and one in reciprocal space).

Metal Complex Model. *Ab-initio* molecular orbital calculations with the STO-3G basis set were performed on $Co(NH_3)_6$ (III) and (II), $Ru(NH_3)_6$ (III) and (II), $Co(en)_3$ (III) and (II), $Co(sep)$ (III and II), and $Co(bpy)_3$ (III) and (II) using the quantum mechanics software package Spartan program.[34] The parameters (UFF) for eq 6 are listed in Table 2.

The basis functions used for the metal complexes were the STO-3G basis set. The Gaussian exponents α and linear expansion coefficients *d* have been chosen as least-squares fits to Slater orbitals with exponent ζ = 1. The standard valence-

TABLE 3: Atomic Charge of Co(NH₃)₆³⁺ and Ru(NH₃)₆³⁺

atom	$Co(NH_3)_6^{3+}$	$Ru(NH_3)_6^{3+}$
M (Co or Ru)	1.574	1.136
N	−0.740	−0.682
H	0.328	0.336
H	0.323	0.333
H	0.329	0.334

TABLE 4: Atomic Charges of Co(en)₃³⁺ and Co(bpy)₃³⁺

atom	charge (*e*)	atom	charge (*e*)
	$Co(en)_3^{3+}$		$Co(bpy)_3^{3+}$
Co	1.063	Co	−1.177
N1	−0.315	N	0.265
H2	0.220	C1	0.135
H3	0.251	C2	−0.162
N4	−0.290	C3	0.107
H5	0.215	C4	−0.098
H6	0.251	C5	−0.031
C7	−0.025	H6	0.138
H8	0.115	H7	0.107
H9	0.080	H8	0.124
C10	−0.061	H9	0.128
H11	0.120		
H12	0.087		

shell scale factor ζ_{3d} for cobalt complexes was set to be 4.10, and ζ_{4d} for ruthenium complexes was set to be 3.20. The detailed method of these STO-3G minimal basis sets for first- and second-row transition metals is found in a previous work by Pietro et al.[35] The use of the STO-3G basis functions for transition metal complexes such as Ru(bpy)₃²⁺ and Co(en)₃³⁺ was also found in the earlier work by Sato et al.[36] They also used the effective charge data from this STO-3G *ab-initio* calculation to study some experimental results of clay−metal complex adsorption.

The atomic charges of the metal complexes from this *ab-initio* molecular orbital calculation include the molecular electrostatic potential (MEP) fitting scheme.[37,38] MEP represents the energy of interaction between a point (positive) charge and the nuclei and electrons of a molecule. For a point positive charge located at p this is given by

$$\epsilon_p = \sum_A^{nuclei} \frac{Z_A}{R_{Ap}} + \sum_\mu^N \sum_\nu^N P_{\mu\nu} \int \frac{\phi_\mu^*(1)\,\phi_\nu(1)}{r_{1p}}\,dx_1\,dy_1\,dz_1 \quad (7)$$

where the first summation is over the nuclei A with charges (atomic numbers) Z_A and separated from p by distances R_{Ap}, and the second (double) summation is over the entire set of N atomic basis functions. $P_{\mu\nu}$ are elements of the one-electron density matrix, which is derived from the Hartree−Fock wave function, and the integrals involve the operator $1/r_{1p}$, the separation between electron 1 and the test charge p. The computed atomic charges of Co(NH₃)₆(III), Ru(NH₃)₆(III), Co-(en)₃(III), and Co(sep) (III) and (II) are shown in Tables 3−5.

Simulation Methods. The montmorillonite clay surface was set to be rigid throughout both energy minimization and molecular dynamics calculations. This is justified by the fact that we are only taking part of the clay structure in the unit cell and the fact that the number of component atoms in the metal complex is well exceeded by that of the clay model. Full atomic motion was allowed for the corresponding freely moving metal complex. Lattice minimization was followed by the molecular dynamics simulation in each metal complex−clay system.

Minimization. Lattice minimization of the metal complex within the system was performed with basal spacing of 20 Å (the vertical distance between octahedral aluminum layers of bottom clay surface to other octahedral aluminum layers in upper clay surface). Each single-metal complex was located in the center of the unit cell for the simulation.

TABLE 5: Atomic Charges of Co(sep)

atom	position	Co(sep)²⁺	Co(sep)³⁺	atom	position	Co(sep)²⁺	Co(sep)³⁺
N	1	0.021	−0.011	H	24	0.100	0.126
Co	2	0.139	0.605	H	25	0.108	0.141
N	3	−0.105	−0.136	H	26	0.120	0.144
N	4	0.055	0.021	H	27	0.120	0.151
N	5	−0.076	−0.109	H	28	0.102	0.123
N	6	0.062	0.025	H	29	0.121	0.154
N	7	0.075	0.044	H	30	0.102	0.128
N	8	−0.357	−0.326	H	31	0.078	0.112
N	9	−0.320	−0.291	H	32	0.104	0.120
C	10	−0.008	−0.037	H	33	0.092	0.127
C	11	−0.016	−0.044	H	34	0.111	0.134
C	12	−0.087	−0.109	H	35	0.082	0.115
C	13	−0.252	−0.260	H	36	0.079	0.099
C	14	−0.039	−0.058	H	37	0.066	0.104
C	15	−0.161	−0.172	H	38	0.108	0.143
C	16	−0.050	−0.066	H	39	0.089	0.112
C	17	−0.056	−0.077	H	40	0.118	0.144
C	18	−0.219	−0.227	H	41	0.114	0.146
C	19	−0.105	−0.126	H	42	0.107	0.132
C	20	−0.054	−0.078	H	43	0.113	0.145
C	21	−0.063	−0.087	H	44	0.120	0.143
H	22	0.113	0.137	H	45	0.097	0.131
H	23	0.087	0.122				
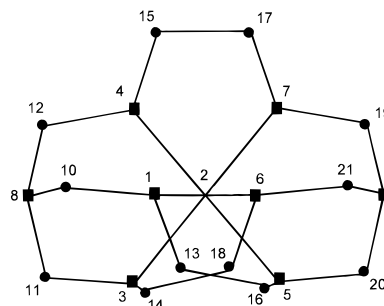
Numbering scheme for Co(sep)²⁺ and Co(sep)³⁺

● Carbon
■ Nitrogen

A conjugated-gradient 200 algorithm was employed for 3000 steps.[39] The vacuum permitivity of $\epsilon_0 = 1.0$ was used for the in-vacuo circumstances throughout the computation. The convergence of the minimization was obtained when root mean square force (RMS force) is less than 0.1 (kcal/mol)/Å.

Molecular Dynamics Calculation (MD). We have used the same procedure for all metal complexes. An isothermal equilibrium dynamics ensemble was chosen. The constant volume and constant temperature condition was used for all metal complex systems throughout the dynamics time span. The number of resulting pair interactions was 37 755 for cobalt sepulchrate complexes, 27 916 for cobalt ethylene diamine complexes, 18 734 for ruthenium hexamine complexes, and 45 300 for cobalt tris(bipyridine) complexes. The pair list was updated every 50 steps. The time step used in the dynamics was 1 fs (0.001 ps) because the system always includes the hydrogen atoms where the fastest motions (hydrogen stretches) have periods of 0.01 ps.[40] The time step must be significantly smaller (about a factor of 10) than the fastest local motion for the numerical integration of Newton's equations of motion to be stable, that is, to generate a reliable molecular dynamics trajectory. The temperature of the system was maintained constant at 300 K by coupling it with a Hoover thermal bath.[41] MD calculations were performed for 70 ps on the whole system.
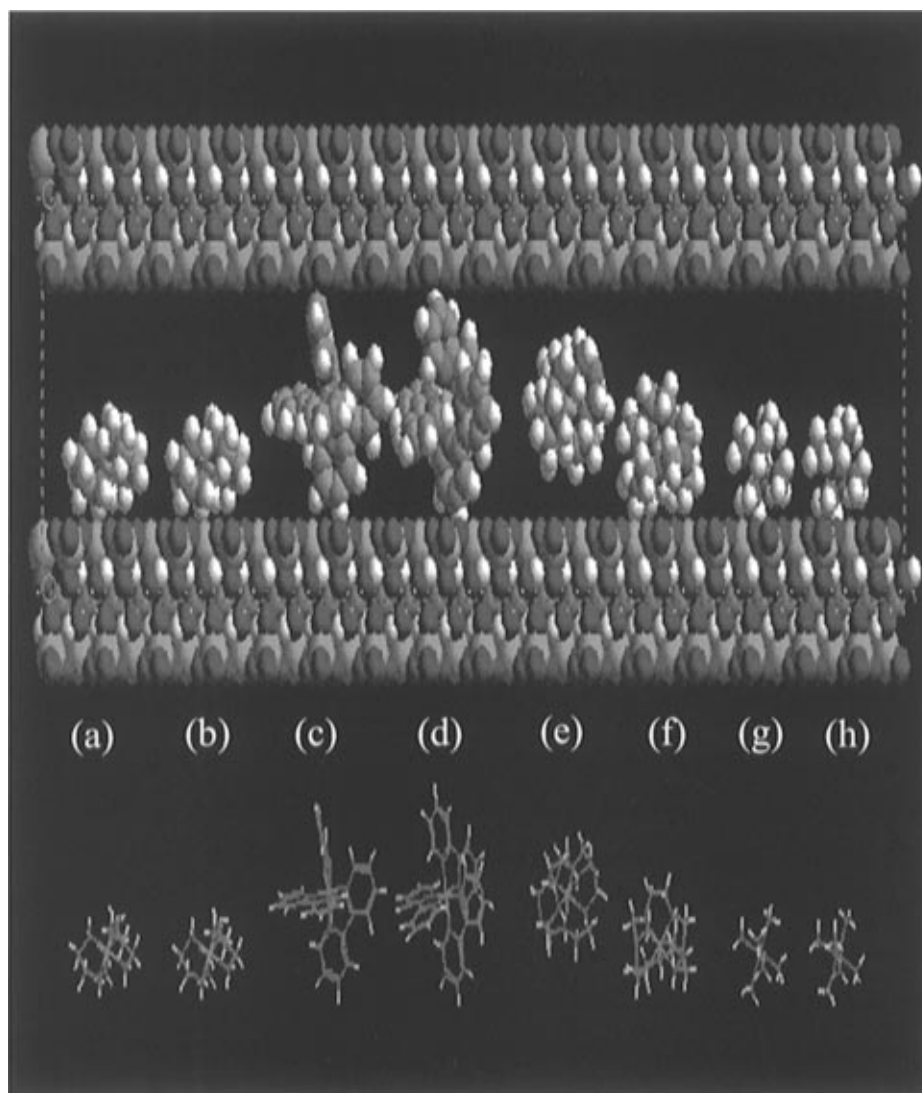
Figure 3. MD-derived snapshots of the complexes at the clay surface: (a) $Co(en)_3^{3+}$, (b) $Co(en)_3^{3+}$, (c) $Co(bpy)_3^{3+}$, (d) $(bpy)_3^{3+}$, (e) $Co(sep)^{2+}$, (f) $Co(sep)^{3+}$, (g) $Ru(NH_3)_6^{2+}$, (h) $Ru(NH_3)_6^{2+}$. The minimized distances between the metal center of the complex and the clay surface are 3.88, 3.80, 6.88, 6.70, 6.71, 4.10, 3.72, 3.61 Å, respectively from a to h.

In the first 14 ps, the system was gradually heated by performing MD runs of 2.0 ps at the following temperatures: 10, 50, 100, 150, 200, 250, and 300 K. In all simulations a constant energy value was obtained within the 2.0 ps run. Another 56 ps of constant volume and constant temperature dynamics was performed at 300 K and used for data analysis.

Results and Discussion

Computational Results from Energy Minimizations. The minimized energy computations result from an *ab-initio* calculation of charge distribution on the molecule (Tables 3−5) and a summation of the charge iteration between each atom in the system (eq 4). In general, the larger the computed radius of the compound, the smaller the total energy and the smaller the electrostatic component.

Figure 3 provides a graphical display of these observations. The minimized energy configurations of the compounds are displayed. $Co(sep)^{2+}$ and $Co(sep)^{3+}$ show significant difference in spatial orientation and relative distance from the clay surface. The distances between the metal atom center and the clay surface are also shown in the caption of Figure 3. The distance does not follow the trend in size of the probe molecule directly, but depends on the force field applied through the available space within the limited interlayer gap. Note that $Co(bpy)_3^{n+}$ complexes do not have as much space as other complexes in

TABLE 6

complex	r (Å)	energy (kcal/mol)			$E_3 - E_2^b$	CEC^c (mequiv/g)	$E^{\circ d}$ (mV)
		total	vdW^a	electro-static			
Mg^{2+}						0.74	
$Co(NH_3)_6^{3+}$	2.5	112.5	−4.58	117.02		0.703	
$Ru(NH_3)_6^{3+}$	2.68	−311.6	−4.7	−491.6	−210	0.840	−25
$Ru(NH_3)_6^{2+}$	2.67	−290.0	−8.7	−281.3			
$Co(en)_3^{3+}$	3.81	−491.5	−11.7	−479.7	−206	0.304	−10
$Co(en)_3^{2+}$	3.77	−289.0	−15.1	−247.0			
$Co(sep)^{3+}$	3.77	−488.7	−21.7	−467.0	−281	0.078	−35
$Co(sep)^{2+}$	3.77	−201.8	−15.5	−186.3			
$Co(bpy)_3^{3+}$	5.79	−381.7	−30.5	−351.2	−161	0.069	+10
$Co(bpy)_3^{2+}$	5.77	−79.9	19.6	−190.5			

^{a} vdW = van der Waals. ^{b} Difference in calculated electrostatic energy (column 5) between divalent and trivalent complex. ^{c} CEC = cation exchange capacity from ref 13. ^{d} E° is the difference in measured formal potentials for the complex in an aqueous solution and in the clay ($E^{\circ}_{soln} - E^{\circ}_{clay}$).[13]

the direction that is perpendicular to the clay surface. Therefore minimization of these complexes most likely involves rotation of molecule instead of translational steps.

The computed total energies are 100 s of kcal/mol, values which exceed realistic interaction energies. This is likely due to the use of a dielectric model for the water in the interlayer. We chose the continuum model as there has been some debate over the nature of the dielectric constant near the clay charged
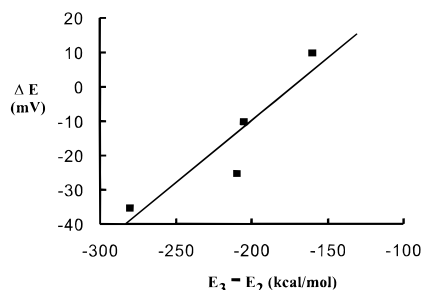
Figure 4. Plot of measured ΔE° as a function of calculated $\Delta\Delta G$.

surface. Consequently, in all subsequent discussions focus will be on trends in energies across the class of compounds as opposed to comparisons of individual energies with measured values.

The equilibrium measured interaction of these compounds with the clay contains other energetic components such as ion–ion pairing, probe–probe pairing, probe–clay hydrogen bonding, and hydrophobic driving forces. Consequently, it is not surprising that the computed trends in energy do not follow the trends in the measured adsorption of these complexes. The measured values for equilibrium adsorption are given in Table 6 in the column labeled cation exchange capacity, CEC (mequiv/g).[13] This number represents the displaceable amount of the complex. For Mg^2, saturation of the clay with the ion and subsequent removal result in a displaceable Mg^{2+} ion content of 0.74 mequiv/g, the reference cation exchange capacity of the clay. The ions $Ru(NH_3)_6^{3+}$ and $Co(NH_3)_6^{3+}$ are completely

exchangeable, indicating that the mechanism of retention of these ions at equilibrium is similar to that of the simple monoatomic cations. While the remaining three cations would be predicted, on the basis of an electrostatic computational model, to have equivalent or higher exchangeabilities with lower interaction energies, the equilibrium experimental data show that the extent of retention increases with ion size. This indicates that the equilibrium mode of retention is not electrostatic in nature, but is driven by the other factors mentioned: ion–ion pairing, probe–probe pairing, probe–clay hydrogen bonding, and hydrophobic driving forces (see Figure 1).

This might suggest that the computations based on a single molecule approaching the clay surface in a dielectric continuum model shed little light on real world processes. This is true if we confine our attention to equilibrium processes. If we look at nonequilibrium data, one finds that the computational model accurately predicts the behavior of these probes. Consider a probe molecule that has been sucked into the electric field of the clay. It can continue to travel within the electric field in response to a diffusion gradient across the clay, or it can come to equilibrium with the clay surface. In Figure 1 this would be a transfer from the channel to a pocket. The rate of equilibrium will be determined in part by the microscopic details of its molecular structure. Thus, if the clay film is small enough, and the rate of equilibration is slow enough, the measured flux of the probe across the film will depend upon the electrostatic component of the interaction of the probe molecule with the clay surface.
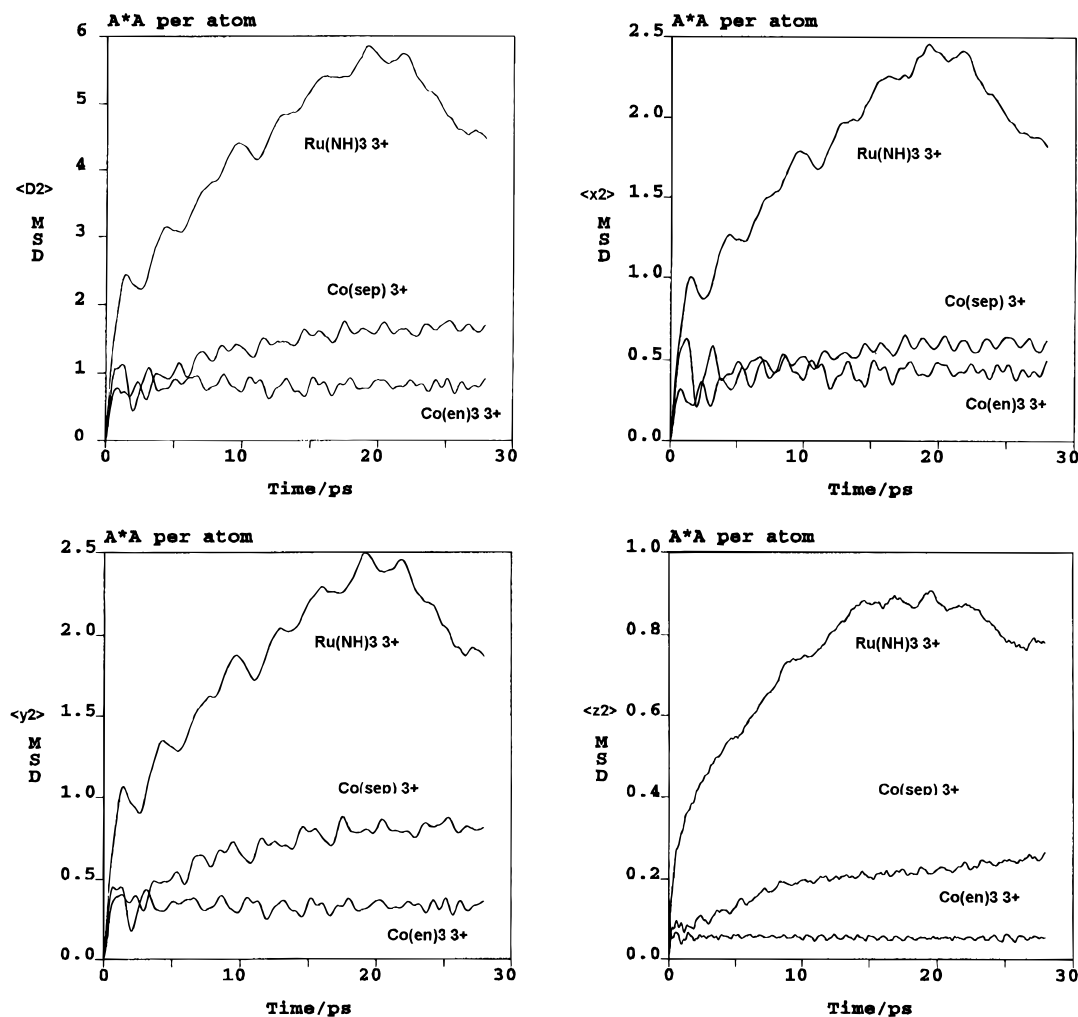

Figure 5. Mean square displacement of the central atom for (1) $Ru(NH_3)_6^{3+}$, (2) $Co(en)_3^{3+}$, (3) $Co(sep)_6^{3+}$: (a) isotropic MSD, $\langle D^2 \rangle$, (b) $\langle x^2 \rangle$, (c) $\langle y^2 \rangle$, and (d) $\langle z^2 \rangle$.
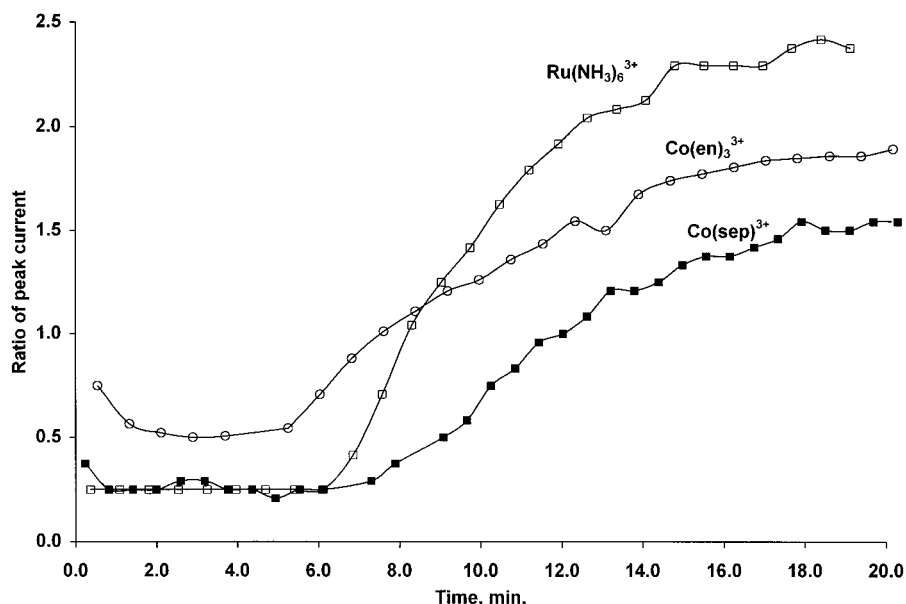
Figure 6. Plot of the reduction currents obtained at the clay-modified electrode normalized by the currents at the bare electrode as a function of time. A magnitude of 1 indicates that the current at the clay-modified electrode is unaffected by the presence of clay.

Under such nonequilibrium conditions, the reduction/oxidation potentials will be perturbed by the variable interaction of the trivalent and divalent species with the electric field of the clay. The redox potentials obtained under nonequilibrium conditions are shown in Table 6. The difference (ΔE°) between the potential measured under solution conditions (E°_{soln}) and that obtained under nonequilibrium conditions in the clay (E°_{clay}) is shown in Table 6. The electrochemical signal associated with the reduction of complexes

$$Ox\text{-}X_3 + e + Na^+ = Red\text{-}X_2 + NaX \qquad (8)$$

within the clay can be expressed in the following Nernst equation:[42,43]

$$E = E^\circ - RT/nF \ln([NaX]/[Na^+]) - RT/nF \ln(K_{III}/K_{II}) - RT/nF \ln([Red\text{-}X_2]/[Ox\text{-}X_2]) \quad (9)$$

where Red-X_2 is the clay-associated reduced species, Ox-X_3 is the clay-associated oxidized species, R is the natural gas constant, T is the temperature, n is the number of electrons involved in the oxidation reduction process, F is the Faraday's constant, NaX is the sodium-filled clay sites, K_{III} is the equilibrium constant associated with the exchange of the trivalent species with sodium-saturated clay, and K_{II} is the equilibrium constant associated with the exchange of the divalent species with the sodium-saturated clay.

The formal potential for the exchange process in the clay is given by the first three terms within eq 9:

$$E^\circ_{cme} = E^\circ - RT/nF \ln([NaX]/[Na^+]) - RT/nF \ln(K_{III}/K_{II}) \quad (10)$$

If the number of exchange sites occupied by sodium are constant, as might be expected to occur just as the clay is filling or as the clay has reached nearly full saturation, and if the concentration of sodium is constant, then

$$\Delta E_{complex} = E^\circ - E^\circ_{cme} = RT/nF \ln(K_{III}/K_{II}) \quad (11)$$

or

$$nF\Delta E_{complex} = RT \ln K_{III} - RT \ln K_{II} = \Delta G_{III} - \Delta G_{II} = \Delta\Delta G_{complex} \quad (12)$$

The larger the association of the trivalent species with the clay surface as compared to the divalent species, the larger the negative shift in potential. We can use the difference in the minimized energies ($E_{III} - E_{II}$) as a measure of $\Delta\Delta G$. As a result, eq 12 predicts that reduction potential shift should be proportional to the difference in minimized energies.

Table 6 and Figure 4 show the experimental potential shifts and the differences in minimized energy values. A very nice agreement in the general trend is found. An increase in the difference in electrostatic energies is followed by an increase in the difference in measured potential shifts. These data show very nice predictive pattern between computational studies of cationic probe molecules in an electric field and the electrochemical measurements associated with the reduction/oxidation of those probes.

There is no trend in ΔE° with radii or with change in radii (Table 6). This suggests that nonequilibrium effects between the probe and the planar charged surface are affected not just by overall valence and size but by the distribution of partial charge throughout the molecule. This point is well illustrated by noting the variable distribution of charge in Co(sep) in the trivalent and divalent states (Table 5). In the trivalent state the metal ion has a high negative charge density relative to the metal atom in the divalent complex. Furthermore, 11 of the 12 carbon atoms are differentially charged based on the overall valency of the compound. Charge is distributed back to four of the 8 nitrogen atoms in both complexes. However nitrogens 8 and 9, the exposed nitrogens, are more heavily negatively charged in the divalent complex than in the trivalent. It is this differential distribution of charge that affects the relative change stability of this compound in the clay ($E_3 - E_2$) instead of volume changes (there are none as the radius is constant) or overall charge changes.

Molecular Dynamics Results

Other computational outputs commonly include plots of mean square displacement (MSD) as a function of time:

$$MSD = \frac{1}{n}\sum_{i=1}^{n}\frac{1}{s}\sum_{j=1}^{s}|r_i(t_j) - \langle r_i\rangle|^2 \quad (13)$$

where r_i is the position of ith atom, t_j and jth time step, s the total time of dynamics simulations for analysis, and n the total number of atoms in the molecule.

The solution to the diffusion equation indicates that the displacement along an x, y, or z axis from the origin follows a Gaussian distribution. The second moment of this Gaussian is the mean square displacement (MSD or variance) and is related to the self-diffusion equation via the Einstein relationship:[44,45]

$$MSD = 2dDT \tag{14}$$

where d is the number of spatial dimensions. This relationship has been found to depend upon the density of the system explored. When the density of the system investigated is low, quadratic dependencies on time can develop in the initial phase of simulation. The appropriate correlation of MSD with D would be at longer times (>4 ps). In addition, it is necessary to have nonperiodic boundary conditions within the simulation.[40,46,47]

Mean square displacements (MSD) of the probe molecules are shown in Figure 5. The isotropic mean square displacement (MSD) is denoted by $\langle D^2 \rangle$. The anisotropic components of MSD are shown as $\langle x^2 \rangle$, $\langle y^2 \rangle$, and $\langle z^2 \rangle$. Among these $\langle z^2 \rangle$ is the displacement that is perpendicular to the clay surface, and the other two are for the motion parallel to the clay surface. For all compounds shown in Figure 5, there is a steep initial slope (quadratic dependencies) for all direction of motion. Most displacement is made in the x and y direction, which is parallel to the clay surface. The graphical data following this steep initial slope also show that the diffusional motion mostly occurs parallel to the clay surface. It is also possible to extract the diffusion coefficient (D) from MD simulations in this time period:

$$D_{xx} = \lim_{t \to \infty} \frac{1}{2} d \frac{\langle \Delta x(t)^2 \rangle}{t} \tag{15}$$

where D_{xx} is the diffusional coefficient for the motion along the axes parallel to the x axis, which is parallel to the clay surface. D_{yy} (parallel to the clay surface) and D_{zz} (perpendicular to the clay surface) are also calculated by the same method. Calculated D_{xx}'s for Ru(NH$_3$)$_6^{3+}$, Co(sep)$^{3+}$, and Co(en)$_3^{3+}$ are 2.60×10^{-6}, 0.66×10^{-6}, and 0.11×10^{-6} cm^2/(s atom), respectively. Other parallel diffusion coefficients D_{yy}'s for Ru(NH$_3$)$_6^{3+}$, Co(sep)$^{3+}$, and Co(en)$_3^{3+}$ are 2.53×10^{-6}, 0.91×10^{-6}, and 0.11×10^{-6} cm^2/(s atom), respectively. The perpendicular diffusion coefficients, D_{zz}'s, for Ru(NH$_3$)$_6^{3+}$, Co(sep)$^{3+}$, and Co(en)$_3^{3+}$ are 0.86×10^{-6}, 0.29×10^{-6}, and 0.03×10^{-6} cm^2/(s atom), respectively.

MSD plots have been previously related to measurements of diffusion by macroscopic experiments.[48] It is interesting to note that the diffusional motion represented by the relative magnitude of $\langle x^2 \rangle$ and $\langle y^2 \rangle$ is in the order Ru(NH$_3$)$_6^{3+}$ > Co(sep)$^{3+}$ ∼ Co(en)$_3^{3+}$. This order is observed experimentally (Figure 6). Ru(NH$_3$)$_6^{3+}$ shows the greatest linear increase after the time lag.

These results suggest that MSD computations may be useful in determining the shape of the energy well on the clay surface. It is probable that inclusion of a surface layer of water molecules could provide even more reliable MD results.

References and Notes

(1) Mercier, L.; Detellier, C. *Env. Sci. Technol.* **1995**, *29*, 1318−1323.

(2) Smith, J. A.; Jaffe, P. R.; Chiou, C. T. *Environ. Sci. Technol.* **1990**, *24*, 1167−1172.

(3) Zamzow, M. J.; Eichbaum, B. R.; Sandgren, K. R.; Shanks, D. E. *Sep. Sci. Technol.* **1990**, *25*, 1555−1569.

(4) Shackelford, C. D.; Daniel, D. E.; Liljestrand, H. M. *J. Contam. Hydrol.* **1989**, *4*, 241−273.

(5) Shackelford, C. D.; Daniel, D. E. *J. Geotech. Eng.* **1991**, *117* (3), 485−506.

(6) Shackelford, C. D.; Daniel, D. E. *J. Geotech. Eng.* **1991**, *117* (3), 467−484.

(7) Zen, J.-M.; Jeng, S.-H.; Chen, H.-J. *Anal. Chem.* **1996**, *68* (3), 498−502.

(8) Yuasa, M.; Nagaiwa, T.; Kato, M.; Sekine, I.; Hayashi, S. *J. Electrochem. Soc.* **1995**, *142* (8), 2612−2617.

(9) Ogorevc, B.; Cai, X.; Grabec, I. *Anal. Chim. Acta* **1995**, *305* (1−3), 176−182.

(10) Yan, Y.; Bein, T. *Chem. Mater.* **1993**, *5* (7), 905−907.

(11) Fitch, A.; Du, J.; Gan, H.; Stucki, J. W. *Clays Clay Miner.* **1995**, *43* (5), 607−614.

(12) Fitch, A.; Lee, S. A. *J. Electroanal. Chem.* **1993**, *344*, 45−59.

(13) Fitch, A.; Song, J.; Stein, J. *Clays Clay Miner.* **1996**, *44* (3), 370−380.

(14) Fitch, A.; Subramanian, P. *J. Electroanal. Chem.* **1993**, *362* (1), 177−185.

(15) Edens, G. J.; Fitch, A.; Lavy-Feder, A. *J. Electroanal. Chem.* **1991**, *307*, 139−154.

(16) Fitch, A. In *Access in Nanoporous Systems*; Pinnavaia, T. J., Thorpe, M. F., Eds.; Plenum Press: New York, 1995; pp 93−110.

(17) Fitch, A. *Clays Clay Miner.* **1990**, *38*, 391−400.

(18) Haase, F.; Sauer, J. *J. Am. Chem. Soc.* **1995**, *117*, 3780−3785.

(19) Bremard, C.; Ginestet, G.; Laureyns, J.; Maue, M. L. *J. Am. Chem. Soc.* **1995**, *117*, 9274−9284.

(20) Delville, A. *J. Phys. Chem.* **1995**, *99*, 2033−2037.

(21) Hess, A. C.; Sanders, V. R. *J. Phys. Chem.* **1992**, *96*, 4367−4374.

(22) Keldsen, G. L.; Nicholas, J. B.; Carrado, K. A.; Winaw, R. E. *J. Phys. Chem.* **1994**, *98*, 279−284.

(23) Delville, A. *J. Phys. Chem.* **1993**, *97*, 9703−9712.

(24) Bleam, W. R. *Rev. Geophys.* **1993**, *31* (1), 51−73.

(25) Sato, H.; Yamagishi, A.; Kato, S. *J. Phys. Chem.* **1992**, *96*, 9377−9382.

(26) Stein, J. A.; Fitch, A. *Anal. Chem.* **1995**, *67* (8), 1322.

(27) Sposito, G. *The Chemistry of Soils*; Oxford University Press: New York, 1989.

(28) Maegdefrau, E.; Hoffmann, U. *Z Kristallgr., Kristallgeom., Kristallphys. Kristallchem.* **1937**, 98−299.

(29) Bohn, H.; McNeal, B.; O'Connor, G. *Soil Chemistry*; John Wiley & Sons, Inc.: New York, 1979.

(30) Moore, D. M.; Robert, C.; Reynolds, J. *X-Ray Diffraction and the Identification and Analysis of Clay Minerals*; Oxford University Press: New York, 1989.

(31) Skipper, N. T.; Sposito, G.; Chang, F.-R. C. *Clays Clay Miner.* **1995**, *43*, 285−293.

(32) Skipper, N. T.; Sposito, G.; Chang, F.-R. C. *Clays Clay Miner.* **1995**, *43*, 294−303.

(33) Karasawa, N.; Goddard, W. A. *J. Phys. Chem.* **1989**, *93*, 7320.

(34) *Spartan 3.0 Computer Modeling Software*; Wavefunction, Inc., 1993.

(35) Pietro, W. J.; Hehre, W. J. *J. Comput. Chem.* **1983**, *4*, 241.

(36) Sato, H.; Yamagishi, A.; Kato, S. *J. Am. Chem. Soc.* **1992**, *114*, 10933−10940.

(37) Chirlian, L. E.; Francl, M. M. *J. Comput. Chem.* **1987**, *8*, 894.

(38) Breneman, C. M.; Wiberg, K. B. *J. Comput. Chem.* **1990**, *11*, 361.

(39) Fletcher, R.; Reeves, C. M. *Comput. J.* **1964**, *7*, 149.

(40) *Cerius2 1.0 User's Reference*; Molecular Simulations Inc., 1992; p 152.

(41) Hoover, W. H. *Phys. Rev. A* **1985**, *31*, 1695.

(42) Fitch, A. *J. Electroanal. Chem.* **1990**, *284*, 237.

(43) Naegeli, R.; Redepenning, J.; Anson, F. C. *J. Phys. Chem.* **1986**, *90*, 6227.

(44) Haile, J. *Molecular Dynamics Simulations: Elementary Methods*; John Wiley: New York, 1992; pp 296−297.

(45) Müller-Plathe, F.; Rogers, S. C.; van Gunsteren, W. F. *J. Chem. Phys.* **1993**, *98* (2), 9895.

(46) Dünweg, B.; Kremer, K. *J. Chem. Phys.* **1993**, *99* (9), 6983.

(47) Magda, J. J.; Tirrell, M.; Davis, H. T. *J. Chem. Phys.* **1983**, *83* (4), 1888−1900.

(48) Catlow, C. R. A.; Gale, J. D.; Gay, D. H.; Lewis, D. W. In *Access in Nanoporous Materials*; Pinnavaia, T. J., Thorpe, M. F., Eds.; Plenum Press: New York, 1995.